Design and finite element simulations of aluminium foam-filled thin-walled tubes

A.G. Hanssen*

Department of Structural Engineering,
Structural Impact Laboratory (SIMLab),
Norwegian University of Science and Technology (NTNU),
Trondheim N-7491, Norway
E-mail: arve.hanssen@ntnu.no

SINTEF Materials and Chemistry,
Applied Mechanics and Corrosion,
Trondheim N-7465, Norway
*Corresponding author

A. Reyes, O.S. Hopperstad and M. Langseth

Department of Structural Engineering,
Structural Impact Laboratory (SIMLab),
Norwegian University of Science and Technology (NTNU),
Trondheim N-7491, Norway
E-mail: aase.reyes@ntnu.no
E-mail: odd.hopperstad@ntnu.no
E-mail: magnus.langseth@ntnu.no

Abstract: This paper presents experiences gained at SIMLab in modelling and design of aluminium-foam-filled tubes for structural applications. The main challenges for robust finite element simulations using explicit codes are outlined and references to previous studies are used for illustration. Any details whatsoever may be found in the original papers referenced in the text.

Keywords: aluminium extrusions; aluminium foam; energy absorption; crash box; LS-DYNA; finite element; constitutive modelling.

Reference to this paper should be made as follows: Hanssen, A.G., Reyes, A., Hopperstad, O.S. and Langseth, M. (2005) 'Design and finite element simulations of aluminium foam-filled thin-walled tubes', *Int. J. Vehicle Design*, Vol. 37, Nos. 2/3, pp.126–155.

Biographical notes: Arve Grønsund Hanssen received his Doctoral degree in 2000 at the Norwegian University of Science and Technology. He is currently employed by SINTEF and the Norwegian University of Science and Technology. His work is related to prediction of structural behaviour during accidental loading using non-linear finite element simulations.

Aase Gavina Reyes received her Doctoral degree in 2003 at the Norwegian University of Science and Technology (NTNU). Her thesis was entitled 'Oblique loading of aluminum crash components'. She is now a post doc at the Department of Structural Engineering at NTNU. Her research focus is on constitutive modelling of metallic materials with emphasis on fracture initiation and propagation within the framework of the finite element method.

Odd Sture Hopperstad received his Doctoral degree in Structural Engineering at the Norwegian Institute of Technology in 1993. He is now Professor of Structural Engineering at the Norwegian University of Science and Technology. His fields of interests are within mathematical modelling of structural materials, nonlinear finite element methods, and structural analysis and design. He is presently involved in research activities on crashworthiness of light structures, structural impact, modelling of material behaviour and fracture, and forming and formability of aluminium extrusions.

Magnus Langseth is Professor of Aluminium Structures at the Norwegian University of Science and Technology. Langseth is the author of more than 60 papers in international journals and more than 70 papers at international conferences. These publications are manly worked out together with the 11 PhD students he has supervised in the period 1990–1999, and the nine PhD students he at present is supervising. Topics for his research have been accidental loads in the offshore industry with special emphasis on dropped objects (topic of his dr. ing. thesis), forming of aluminium components and stability of plated aluminium structures. His present research activities are primarily related to impact and crashworthiness of aluminium, magnesium and high-strength steel structures as well as light-weight ballistic protection.

1 Introduction

Research on aluminium foam accelerated at the end of the 1990s. Aluminium foam is a structural material where the density of the foam directly controls the mechanical properties, such as strength. A number of production processes exists, see Banhart (2001).

The Al-foam filling of thin-walled tubes, such as sections made from steel sheets or aluminium extrusions, presents practical as well as finite-element simulation related challenges. Practical challenges comprise ease of manufacture, joining technology, tolerances and repeatability in material properties, among others. Here, the need for practical easy-to-use design formulas may also be imminent. On the other hand, the following questions are usually addressed for finite element simulations: What material model should be used for the aluminium foam? How should the bonding between foam and tube be modelled? How can the thin layer of skin on the foam be modelled? Even if the relevant modelling techniques are close at hand, the identification can be a problem due to lack of material data. In many cases, a full validation test programme may be the best solution in order to obtain a reliable model, Figure 1.

Figure 1 Challenges in modelling of foam-filled tubes

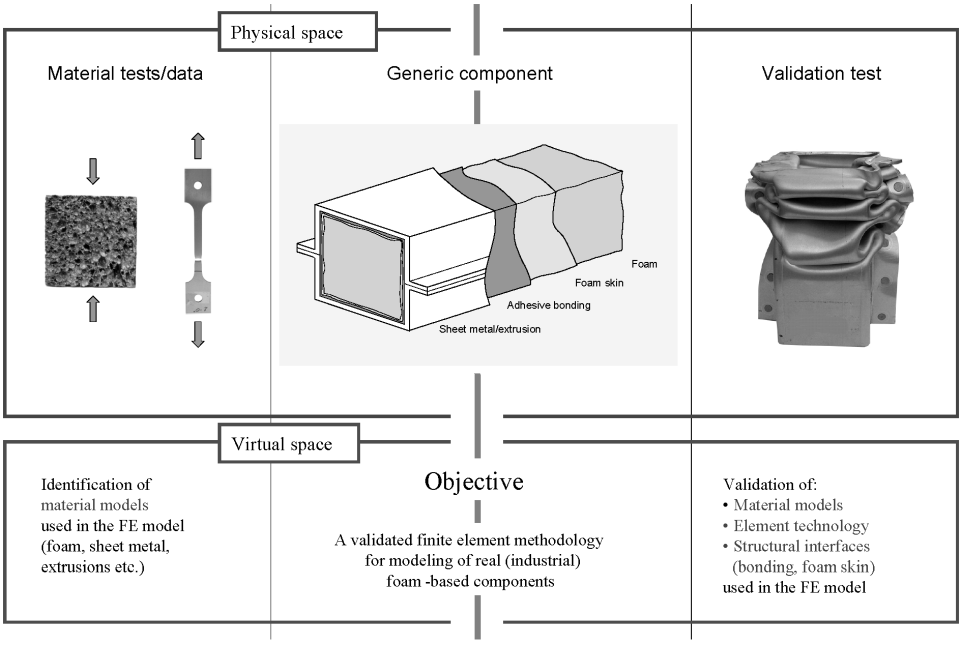

The following sections will focus on the description of mechanical properties of aluminium foam, design formulas for foam-based structural components and recommendations for finite element simulations. All aspects are given from an engineer's point-of-view. Section 2 presents simple formulas for predicting the strength of aluminium foam from the foam density and shows how surface skin of foam can be taken into account in bending of a foam-based member. Section 3 recapitulates design formulas which may be used for energy absorbing applications, such as axial crushing and oblique loading of foam-filled extrusions and behaviour of foam-filled sections in pure bending. Section 4 gives an overview of finite element modelling of foam-based components.

2 Description of foam properties

2.1 Uniaxial static crushing

Aluminium foams are presently being regarded with interest concerning the controlled absorption of kinetic energy, i.e. for crashworthiness applications. An explanation to this can be sought in Figure 2, where generalised compressive as well as tensile properties of a cube of aluminium foam are depicted. The compressive behaviour is characterised by an initial elastic region followed by what is commonly referred to as the plateau region, identified by a more or less constant stress level for strains up to 50–80%. The average stress level of this region is referred to as the plateau stress σ_f. Further compression of the foam will lead to compaction, quantified by the densification strain ε_D, Figure 2. In addition, due to the low weight of the foam, it is the constant stress levels in the plateau region that promotes the use of the foam for energy absorption purposes. Hence, kinetic

energy can be absorbed at specified force levels, ensuring the integrity of valuable goods as well as the people in the passenger cell of a colliding car.

Figure 2 Generalised compressive and tensile properties of aluminium foam

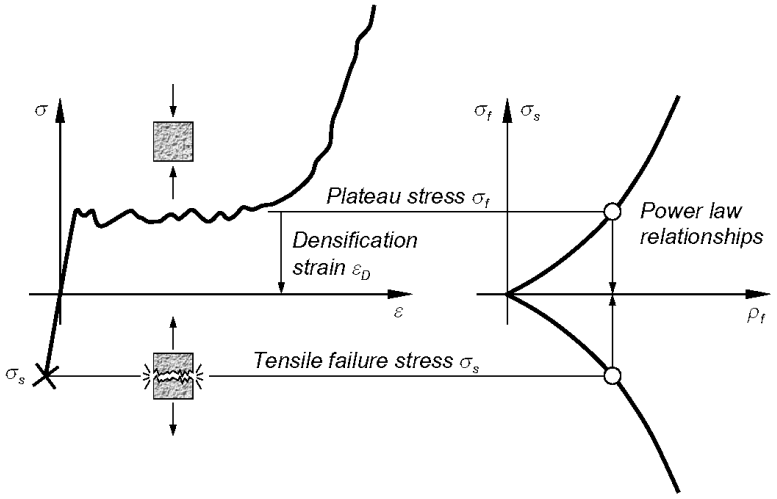

Another characteristic of the aluminium foam is the dependency of mechanical properties on the density of the foam. This is referred to as power law relationships, Figure 2, and for the plateau stress σ_f can be approximated by

$$\sigma_f = C_p \left[\frac{\rho_f}{\rho_{f0}} \right]^n \tag{1}$$

where ρ_f is the foam density and ρ_{f0} the density of the base material (2.7 g/cm^3). C_p and n are material constants found by model calibration with uniaxial compression tests of foam cubes. For the continuously casted aluminium foam produced by Hydro Aluminium (now called SAF – Stabilised aluminium foam, produced by CYMAT), typical values of C_p and n are 450 MPa and 2.0 respectively. The corresponding density range of this foam is from 0.15 to 0.50 g/cm^3.

In tension, the behaviour is quite different from that in compression. The initial elastic region is followed by brittle failure, characterised by the tensile failure stress σ_s. The tensile capacity σ_s of the Hydro foam is approximately equal to the plateau stress σ_f, i.e. they both have roughly the same foam density dependency.

Dividing equation (1) by the foam density ρ_f yields the mass specific energy absorption E_M (destroyed mass)

$$E_M = \frac{\sigma_f}{\rho_f} = \frac{C_p}{\rho_{f0}} \left[\frac{\rho_f}{\rho_{f0}} \right]^{n-1} . \tag{2}$$

An important consequence of this expression is that the mass specific energy absorption of the foam increases with the foam density as long as $n > 1$. Hence, solely from this point of view, high foam densities are preferable when minimum weight designs are considered.

2.2 Uniaxial dynamic crushing

For crashworthiness applications it is relevant to assess the influence of dynamic loading conditions on the mechanical properties. Several papers address this issue, among them are Tan and Reid (2000), Deshpande and Fleck (2000a) and Lopatnikov et al. (2003). Tan and Reid (2000) showed that the maximum dynamic enhancement of the plateau stress of aluminium foam could be approximated by a shock wave theory, giving

$$\sigma_f^D = \sigma_f + \frac{\rho_f}{\varepsilon_D} v^2 \tag{3}$$

where σ_f^D is the dynamic plateau stress and v is the loading velocity.

2.3 Three-point bending and the effect of surface skin

The manufacturing process of aluminium foam generates a surface layer of dense aluminium, generally referred to as the surface skin. It may be important to take into account the thickness of this skin for design and finite element simulations. Hanssen et al. (2003) suggested to use three-point-bending tests on IFAM foam blocks to find the computational-equivalent skin (CES) thickness of such components. Here, three types of tests were prepared for the three-point-bending set-up,

- foam blocks with no surface skin
- foam blocks with surface skin on all sides
- foam blocks where the skin on the tensile flange was removed.

These components are referred to as 0S, 4S and 3S respectively, see Figure 3. The surface skin was removed by machining. Three parallel tests were done for each class of component. Figure 4 shows the tests results. The pure foam block (0S) has the lowest capacity as opposed to the block with surface skin on all four sides (4S). Scatter is evident both in ultimate capacity and ductility. This is probably related to the inhomogeneous nature of the surface skin.

Figure 3 Samples for three-point-bending tests and schematic of test-set up

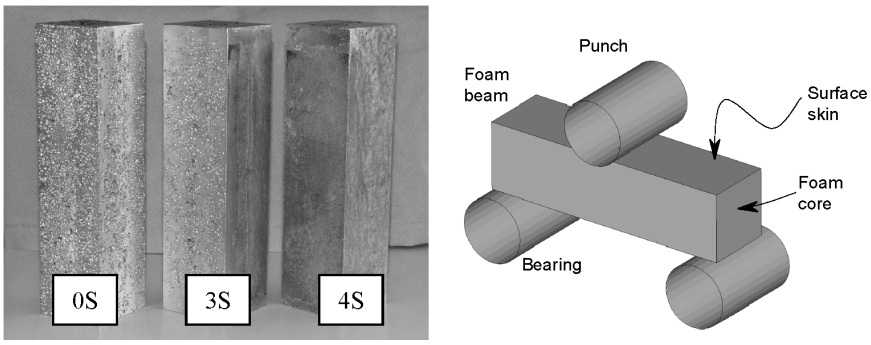

0S: skin totally removed; 3S: skin removed on the tensile flange; 4S: as produced.

Figure 4 Results from three-point-bending tests, punch force F vs. punch displacement w

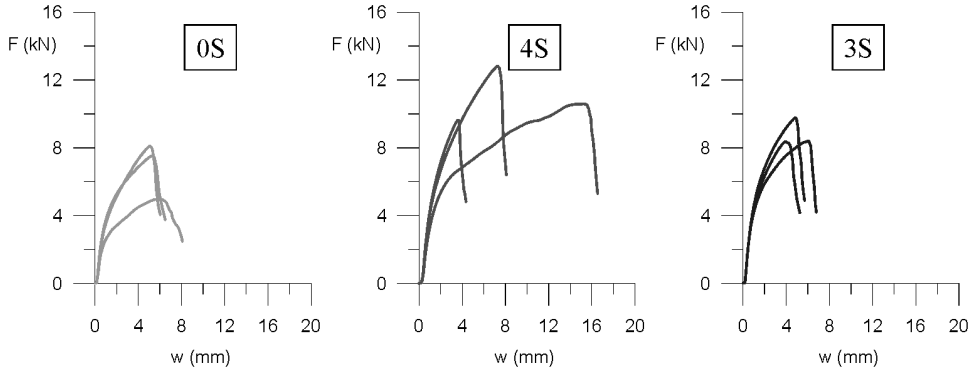

Moreover, Hanssen et al. (2003) used the following procedure in order to obtain a value for the CES thickness. Consider a square, foam-filled cross section of width b and skin thickness equal to h (CES). The material of the surface skin is fitted to a bilinear hardening curve defined by

$$\begin{aligned} &\sigma = E\varepsilon, \quad \sigma < \sigma_{02} \\ &\sigma = \sigma_{02} + E_t\left(\varepsilon - \frac{\sigma_{02}}{E}\right), \quad \sigma \geq \sigma_{02} \end{aligned} \tag{4}$$

where σ is the nominal stress, σ_{02} is the yield stress, E is the Young's modulus, E_t is the tangent modulus and ε is the nominal strain. Let $M = M_e + M_{sf}$ be the total moment capacity of the cross section, where M_e is the moment capacity of the surface skin and M_{sf} the contribution from the foam core. The moment contribution from the surface skin as a function of the cross-section curvature κ can be simplified as (Hanssen et al., 2003)

$$\begin{aligned} &\frac{M_e}{M_{02}} = f\left(1 - \frac{E_t}{E}\right) + \frac{E_t}{E}\frac{\kappa}{\kappa_{02}}, \quad M_e > fM_{02} \\ &\frac{M_e}{M_{02}} = \frac{\kappa}{\kappa_{02}}, \quad M_e \leq fM_{02}. \end{aligned} \tag{5}$$

The beam curvature at surface skin yielding κ_{02} is given by

$$\kappa_{02} = \frac{2\sigma_{02}}{Eb}. \tag{6}$$

The section shape factor f is written as

$$f = \frac{M_{pl}}{M_{02}} \tag{7}$$

where the elastic limit moment M_{02} as well as the perfect-plastic reference moment M_{pl} are given by

$$M_{02} = \sigma_{02}\left(bh(b-h) + \frac{(b-2h)^3 h}{3(b-h)}\right), \quad M_{pl} = \sigma_{02}\left(bh(b-h) + \frac{1}{2}h(b-2h)^2\right). \tag{8}$$

Let σ_s be the tensile foam strength. The simple linear-elastic bending resistance of the quadratic foam block M_f is then readily written in the form

$$M_f = M_{sf}\frac{\kappa}{\kappa_s} = \sigma_s \frac{(b-2h)^3}{6} \tag{9}$$

where the last term represents the maximum capacity of the foam block. The curvature κ_s that corresponds to the failure strain ε_s in the foam core can be expressed by

$$\kappa_s = \frac{2\varepsilon_s}{(b-2h)}. \tag{10}$$

Adding the expressions of M_e and M_f (and finally normalising with respect to M_{sf}) gives the total bending moment capacity M of the foam-filled beams as function of curvature κ:

$M = M_e + M_f$, i.e.

$$\begin{aligned} \frac{M}{M_{sf}} &= \left(f\left(1-\frac{E_t}{E}\right)+\frac{E_t}{E}\frac{\kappa}{\kappa_{02}}\right)\frac{M_{02}}{M_{sf}}+\frac{\kappa}{\kappa_s}, \quad M_e > fM_{02} \\ \frac{M}{M_{sf}} &= \frac{\kappa}{\kappa_{02}}\frac{M_{02}}{M_{sf}}+\frac{\kappa}{\kappa_s}, \quad M_e \le fM_{02}. \end{aligned} \tag{11}$$

Assuming that the maximum capacity of the cross section is obtained at foam failure, the maximum bending moment M_s is found from equation (11) when $\kappa = \kappa_s$. From Hanssen et al. (2003), the following parameters were approximated for the skin material; $\sigma_{02} = 115$ MPa and $E_t = 2100$ MPa (linear from ε_{02} to 6% strain). In addition $E = 70000$ MPa. The outer width of the cross section is $b = 53$ mm. From Figure 4 it can be shown that the average ultimate force for component 0S (no skin) is $\overline{F}_{0S} = 6.8$ kN and for component 4S (skin all sides) the same value is $\overline{F}_{4S} = 11.2$ kN. Now, since $M/M_{sf} = \overline{F}_{4S}/\overline{F}_{0S}$ we have that $M/M_{sf} = 1.6$. The only unknown in the above given equations to produce this moment ratio is h. It can be shown that $h = 0.15$ mm satisfies the set of equations; hence the CES thickness is 0.15 mm for this component.

3 Experimental investigations and design formulas

3.1 Pure axial crushing

The sections in Figure 5 are of a statically crushed non-filled extrusion and a similar foam-filled extrusion. As observed, the number of lobes in the sidewalls of the extrusions is increased due to the foam filling. In general, the number of lobes is an increasing function with respect to the foam density. The foam filler causes the initial buckling of the sidewalls to take place on an elastic foundation, thus reducing the buckling length and increasing the number of lobes created. For circular extrusions, an effect of increasing foam density may also be to change the deformation mode, Figure 6.

Figure 5 Non-filled vs. foam-filled square extrusion, quasi-static loading

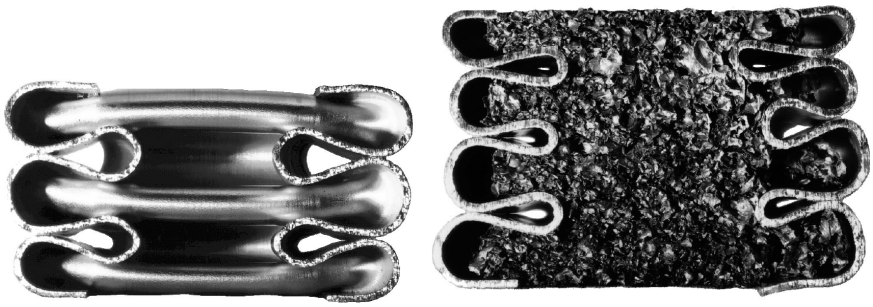

Figure 6 Axial crushing of non-filled and foam-filled circular and square extrusions, quasi-static loading

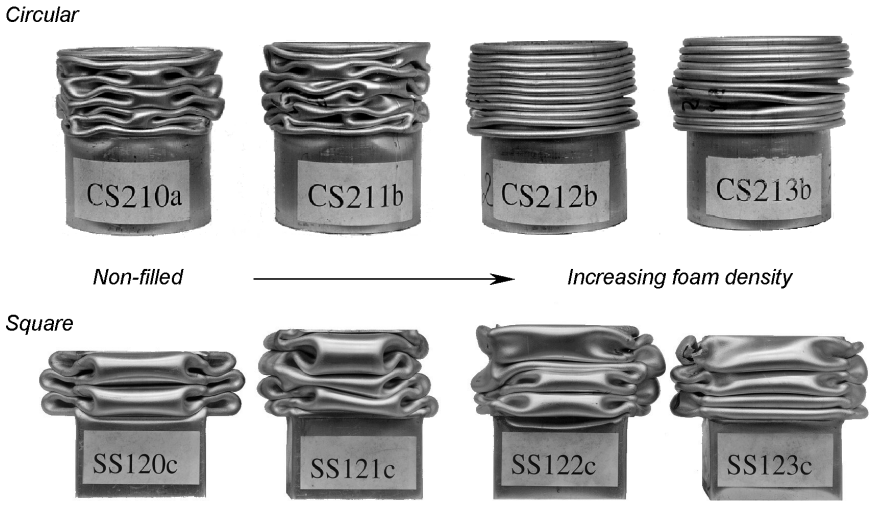

The dynamic loading condition does not significantly alter the apparent deformation behaviour of the square and circular extrusions, although there are some differences. However, a difference between static and dynamic loading conditions can be observed by studying the force vs. deformation curves of tested foam-filled extrusions. Figures 7–9 compare the static with the corresponding dynamic force vs. deformation behaviour of foam alone (Figure 7), a non-filled extrusion (Figure 8) and finally a foam-filled extrusion (Figure 9). A simple means of determining the effect of the loading condition is the ratio between dynamic and static energy absorption. This ratio is referred to as the 'energy ratio' in Figures 7–9 and is plotted as a function of axial deformation. As illustrated in Figure 7, a loading velocity of 15 m/s appears to have no significant effect on the force-deformation behaviour of aluminium foam alone. The contrary is observed when studying the crushing of non-filled extrusions, Figure 8. Here, the force levels are increased significantly. Experiments on the extrusion material discovered no significant strain rate sensitivity; hence the increase in force is likely to be due to transverse inertia forces arising in the extrusion walls during crushing. It was observed that the energy ratio generally was a decreasing function of deformation. Since the strength of the extrusion material can become greater without increasing the material

density, an increase in material strength will lead to a reduction of the relative importance of the dynamic inertia effects (reduced energy ratio). The same effect is observed when filling the extrusion with the rate insensitive foam, Figure 9. The increase in the total force level compared with the non-filled extrusion diminishes the relative importance of the inertia effects of the extrusion sidewalls, leading to a lower energy ratio.

Figure 7 Static and dynamic force deformation curves of circular foam specimens. Specimen diameter: 79 mm; foam density: 0.38 g/cm^3; impact velocity: 15 m/s

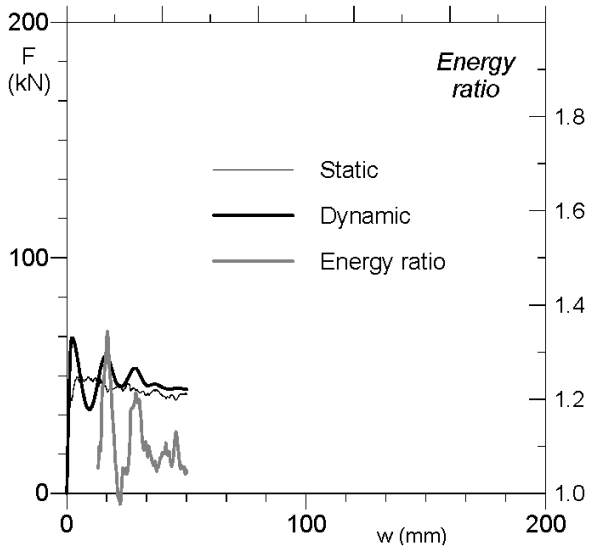

Figure 8 Static and dynamic force deformation curves of square non-filled extrusions. Outer width, b: 80 mm; wall thickness, t: 1.95 mm; foam density, ρ_f: 0 g/cm^3; characteristic stress, σ_0: 151 MPa; impact velocity, v_0: 14 m/s

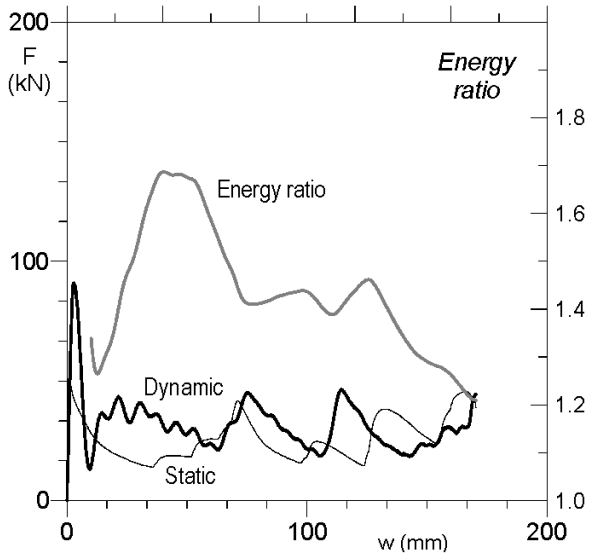

Figure 9 Static and dynamic force deformation curves of square foam-filled extrusions. Outer width, b: 80 mm; wall thickness, t: 1.95 mm; foam density, ρ_f: 0.34 g/cm^3; characteristic stress, σ_0: 151 MPa; impact velocity, v_0: 23 m/s

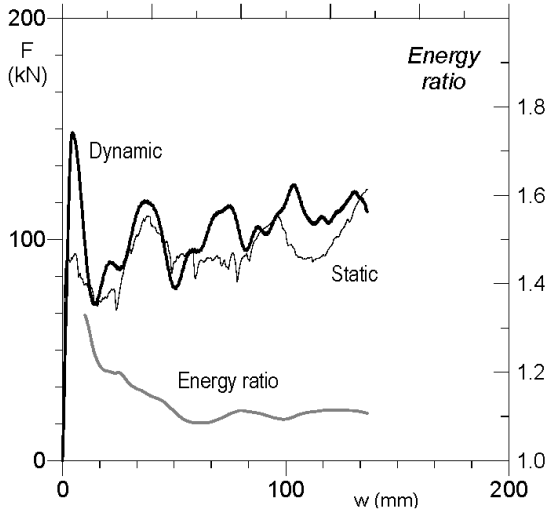

The following empirical design formula has been found to represent the average crush force F_{avg} of both square and circular foam-filled extrusions with satisfactory accuracy

$$F_{\text{avg}} = \overline{F}_{\text{avg}} + \sigma_f A_f + C_1 \sqrt{\overline{\sigma}_0 \sigma_f A}. \tag{12}$$

The first term is simply the average crush force of the corresponding non-filled extrusion, whereas the second term constitutes the uniaxial resistance of the foam filler. As observed experimentally, the average crush force of foam-filled extrusions always exceeds that of the sum of these two terms, see Figure 10. This increase in capacity is referred to as an interaction effect and is represented by the third term in equation (12). The parameters involved are:

Figure 10 Illustration of interaction effect

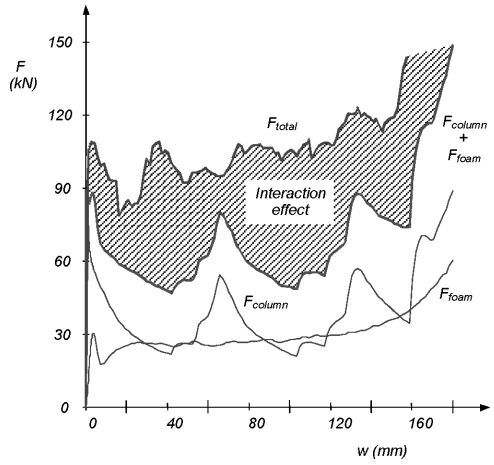

$\overline{F}_{avg}$ average crush force of corresponding non-filled extrusion
σ_f foam plateau stress, see Figure 2
A_f foam core cross-sectional area
C_1 cross-section dependent dimensionless constant, (Table 1)
$\overline{\sigma}_0$ characteristic stress of extrusion material, see Figure 15
A cross-sectional area of extrusion.

In order to make the design formula complete, an expression for the average crush force of non-filled extrusions has been included, see Jones (1989).

$$\overline{F}_{\text{avg}} = C_0 \phi^{2/3} \overline{\sigma}_0 A \tag{13}$$

This equation is represented by the following parameters
C_0 cross-section dependent dimensionless constant (Table 1)
ϕ A/A_f: solidity ratio.

Table 1 Parameters needed for properties of foam-filled tubes. The constants given are based on experimental data

	Square	*Circular*
A_f	$(b-2t)^2$	$\pi(d-2t)^2/4$
A	$4t(b-t)$	$\pi t(d-t)$
ϕ	$4t(b-t)/(b-2t)^2$	$4t(d-t)/(d-2t)^2$
C_0	1.30	2.15
C_1	1.4	0.9
C_2	0.5	0.9
C_3	1.7	17
A_{E0}	0.40 – 0.65*	0.55 – 0.75*
A_{Ef}	0.85	0.85
m	0.8	2
S_E^0	0.76	0.76

*initial peak force neglected.

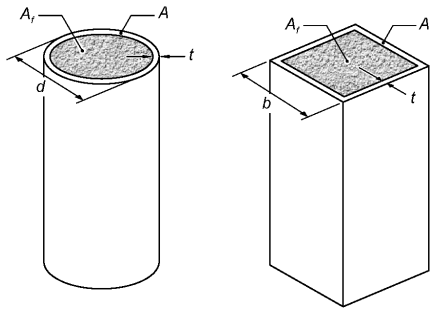

Equation (13) assumes that there is a symmetric deformation pattern for the square extrusions and diamond modes for the circular ones.

By substituting equation (13) into equation (12), the normalised average crush force of foam-filled extrusions can be written as

$$\frac{F_{\text{avg}}}{\bar{\sigma}_0 A} = C_0 \phi^{2/3} + \frac{1}{\phi}\frac{\sigma_f}{\bar{\sigma}_0} + C_1\sqrt{\frac{\sigma_f}{\bar{\sigma}_0}}. \tag{14}$$

The maximum force level $F_{\max}$ occurring during crushing can be approximated by the following expression

$$\frac{F_{\max}}{\bar{\sigma}_0 A} = \frac{1}{A_{E0}} C_0 \phi^{2/3} + \frac{1}{A_{Ef}}\frac{1}{\phi}\frac{\sigma_f}{\bar{\sigma}_0} + C_2\sqrt{\frac{\sigma_f}{\bar{\sigma}_0}} \tag{15}$$

where three new parameters have been introduced:

A_{E0}: ratio between average and maximum force, non-filled extrusion (Table 1)

A_{Ef}: ratio between average and maximum force, foam alone (Table 1)

C_2: cross-section dependent dimensionless constant (Table 1).

A_{E0} and A_{Ef} are referred to as crush force efficiencies, and they can be determined from compression tests on non-filled extrusions and foam alone respectively. If the foam-filled extrusion has a trigger in order to reduce the peak force and initiate folding, see Figure 11, tests on the corresponding triggered non-filled extrusion will yield a value of A_{E0} for use with equation (15). The maximum force of non-filled extrusions is usually related to the initial peak force, even if the extrusions are triggered. Table 1 gives the values of A_{E0} if the initial peak force is neglected, being the equivalent of designing a 'perfect' trigger. Table 1 also gives the minimum value of A_{E0} found for the triggered non-filled components. If tests on the triggered non-filled extrusions are not available for the determination of A_{E0}, it should be possible to utilise the results in Table 1 as a rough guideline for estimation of the maximum force. The crush force efficiency of the foam filler A_{Ef} should be set to 0.85.

Figure 11 Triggers used

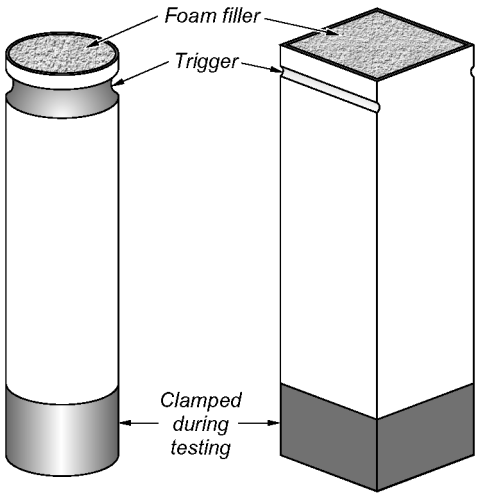

A summary of all the parameters involved in equations (14) and (15) is given in Table 1. Here b is the outer width of the square cross section, d is the outer diameter of the circular extrusion, whereas t represents the wall thickness. It must be noted that the dimensionless constants C_1 and C_2 were found to increase slightly with deformation, Figure 12. The values given in Table 1 correspond to an approximate deformation of 50%. All the constants of Table 1 are based on experimental data and subsequent curve fitting.

Figure 12 Development of C_1 and C_2

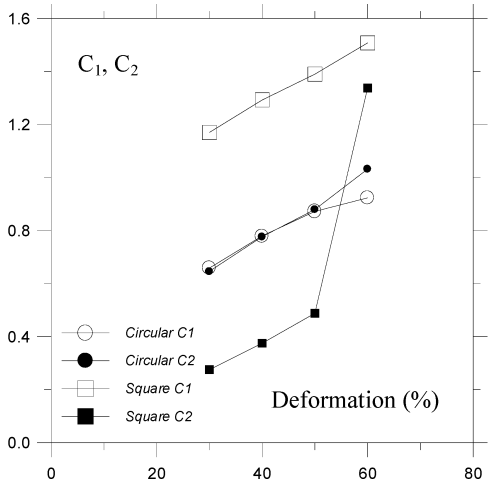

The corresponding correlation plots for equations (14) and (15) vs. experiments are shown in Figures 13 and 14. The diamond and square symbols in Figure 13 represent tests from different series. For most tests, the accuracy of the proposed design formula for the average force is within an error margin of ±10%. The maximum force level is predicted with somewhat less accuracy.

Figure 13 Correlation, average force

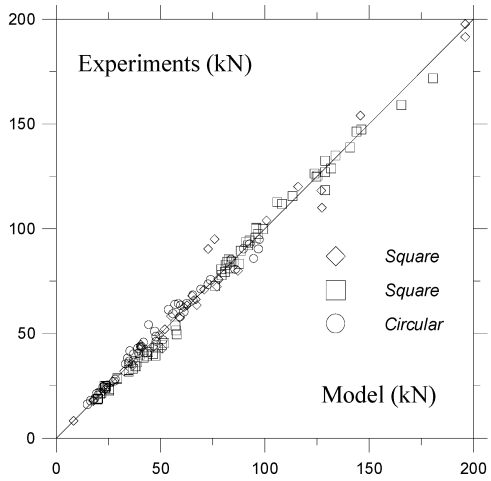

Figure 14 Correlation, maximum force

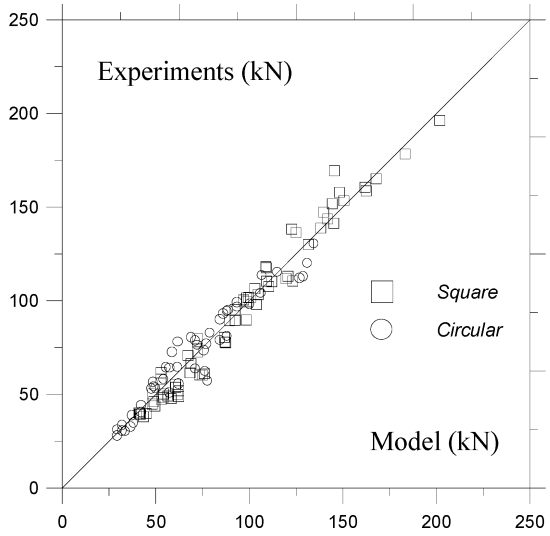

In Table 1, the dimensionless constant C_0 for determination of the average crushing forces of non-filled extrusions is based upon the definition of the characteristic extrusion material stress $\bar{\sigma}_0$ as given in Figure 15. Here $\bar{\sigma}_0$ is defined as the average of the yield stress σ_{02} (0.2% plastic strain) and ultimate stress σ_u. Using this definition, the values of C_0 in Table 1 were determined from correlation with experiments on non-filled aluminium extrusions.

Figure 15 Definition of $\bar{\sigma}_0 = 1/2(\sigma_{0.2} + \sigma_u)$

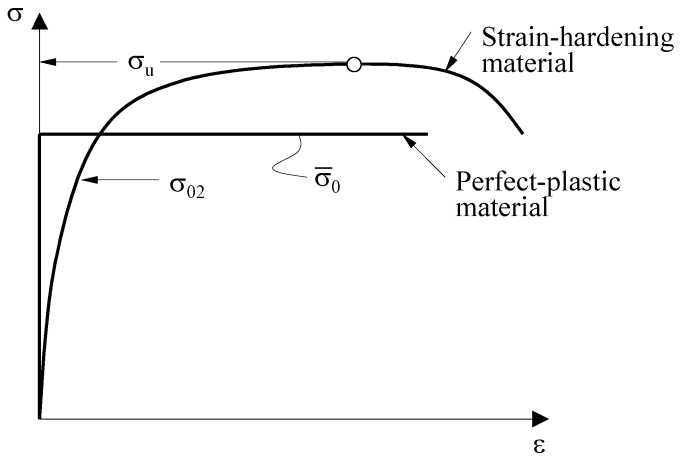

The final design parameter of interest is the effective crushing length of the components, $w_{max} = S_E \times L$. Here S_E is referred to as the stroke efficiency, whereas L is the total length of the component. For a square non-filled extrusion, S_E is approximately 73%, meaning that the component can be crushed three-quarters of its original length before bottoming up occurs (leading to rapidly increasing force levels). When filling foam inside tubes, the

effective crushing length is generally reduced. This has implications for practical design cases, since the total capacity for energy absorption is given by $E = F_{avg} \times S_E \times L$.

The stroke efficiency S_E for a foam-filled extrusion is given by

$$S_E = \frac{\left(C_0 \phi^{2/3} + C_1 \sqrt{\frac{\sigma_f}{\bar{\sigma}_0}} \right) \cdot S_E^F + \frac{1}{\phi} \frac{\sigma_f}{\bar{\sigma}_0} \cdot \varepsilon_D}{C_0 \phi^{2/3} + \frac{1}{\phi} \frac{\sigma_f}{\bar{\sigma}_0} + C_1 \sqrt{\frac{\sigma_f}{\bar{\sigma}_0}}} \tag{16}$$

where

$$S_E^F = S_E^0 (1 - C_3 (\rho_f / \rho_{f0})^m) \quad \text{and} \quad \varepsilon_D = 1 - 1.5(\rho_f / \rho_{f0}). \tag{17}$$

Here ε_D denotes the densification strain of the foam filler. The constants S_E^0, C_3 and m are given in Table 1 for both square and circular extrusions. Figure 16 shows the correlation between this model and experiments.

Figure 16 Correlation, stroke efficiency

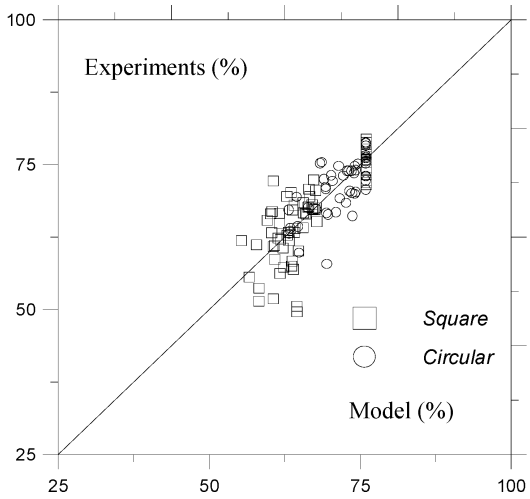

Finally, the total mass of the foam-filled tube is

$$M = (\rho_0 A + \rho_f A_f) \cdot L. \tag{18}$$

The increase in force levels due to dynamic loading conditions is yet to be discussed. For square foam-filled extrusions Hanssen et al. (2000a) assumed that the average force levels of dynamically loaded specimens could be described by modification of equation (12) above. Here, the dynamic effects are accounted for by using the average force term of a dynamically loaded non-filled tube, i.e. $\bar{F}_{\text{avg}}$ in equation (12) is replaced by $\bar{F}_{\text{avg}}^D$.

$$F_{\text{avg}} = \bar{F}_{\text{avg}}^D + \sigma_f A_f + C_1 \sqrt{\bar{\sigma}_0 \sigma_f A} \tag{19}$$

The increase in force levels of the foam-filled component was related to the average crush force of the non-filled extrusion in the following way

$$\bar{F}_{\text{avg}}^{D} = C_0 \phi^{2/3} \bar{\sigma}_0 A \left[1 + C_4 \left(\frac{1}{\phi} \frac{\rho_0}{\bar{\sigma}_0} v_0^2 \right)^{1/2} \right]. \tag{20}$$

Here, the following parameters have been introduced:

ρ_0: density of extrusion material

v_0: initial impact velocity

C_4: factor describing the dynamic effect.

The C_4 parameter was found to be a decreasing function of the relative deformation measure w/l where w and l are defined as

w: deformation

l: half the relative plastic lobe length of a non-filled tube, $l = 0.99 b^{2/3} t^{1/3}$.

Hence, the complete formula giving the average crush force for square foam-filled extrusions subjected to dynamic loading conditions is

$$\frac{F_{\text{avg}}}{\bar{\sigma}_0 A} = C_0 \phi^{2/3} \left[1 + C_4 \left(\frac{1}{\phi} \frac{\rho_0}{\bar{\sigma}_0} v_0^2 \right)^{1/2} \right] + \frac{1}{\phi} \frac{\sigma_f}{\bar{\sigma}_0} + C_1 \sqrt{\frac{\sigma_f}{\bar{\sigma}_0}}. \tag{21}$$

The C_4 factor as a function of w/l was found experimentally (Hanssen et al., 2000a) and is given in Figure 17.

Figure 17 Development of dynamic amplification factor C_4 (square extrusions)

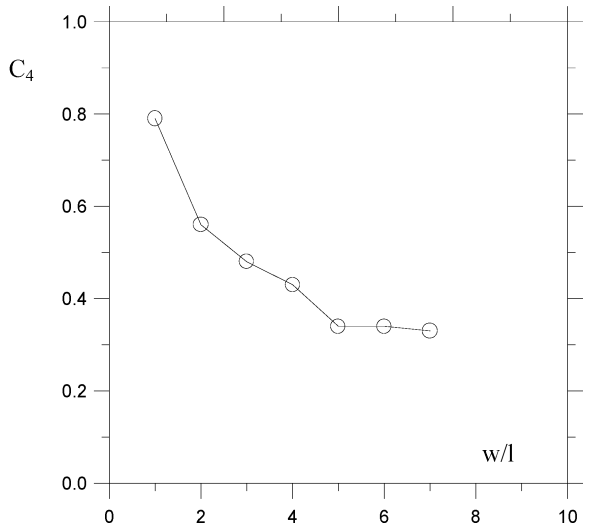

3.2 Oblique loading of axial components

Reyes et al. (2004a) did oblique loading tests on non-filled and foam-filled aluminium AA6060 hollow sections, see Figure 18 for test set-up.

Figure 18 Oblique loading of non- and foam-filled hollow extrusions. Test set-up (left) and typical force-deformation curves for pure axial crushing compared to oblique loading (right) of non-filled components

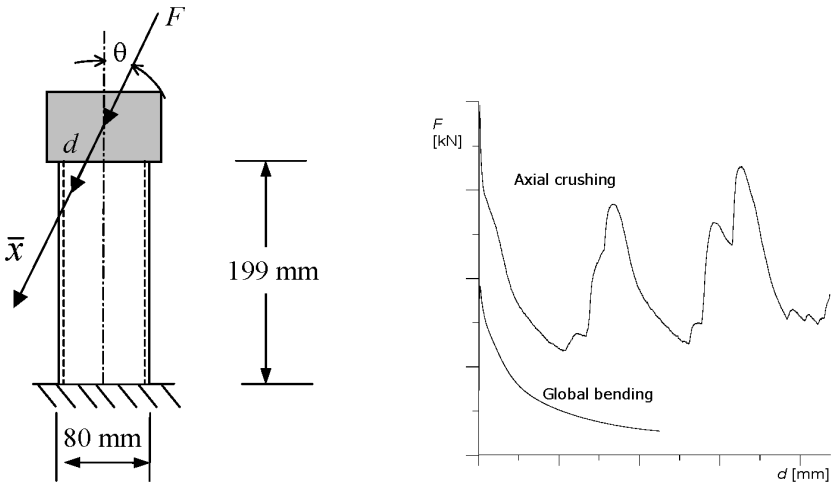

The foam-filled and empty columns developed similar deformation modes in oblique loading. Figure 19 shows three specimens with various foam filler in temper T4 with load angle 5°. Here, the compression flange buckled outward, while the two sidewalls buckled inward. Although the specimens in Figure 19 have the same deformation mode in the sense that the compression wall buckled outward, one can see that there are some differences in the extent of the lobe, which can be considered as a plastic hinge. The lobes in the foam-filled columns are somewhat more localised than in the empty columns, in agreement with the findings of Hanssen et al. (2000a). The foam acts as an elastic-plastic foundation for the sidewalls and reduces their buckling length. A detail of the tube with high-density (0.3 g/cm^3) foam is shown in Figure 20. It is possible to see an indication of a second lobe above the initial lobe. This was also observed for some of the other tubes with high-density foam.

Figure 19 Deformation modes for experiment $\theta = 5°$, temper T4. Empty and foam densities 0.1 g/cm^3 and 0.3 g/cm^3

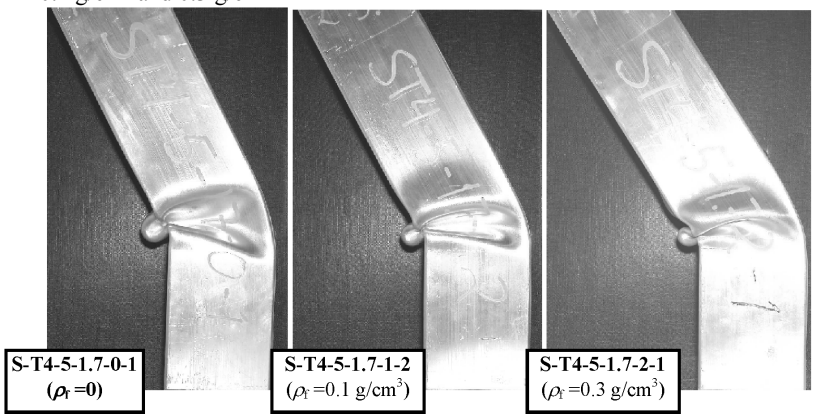

Figure 20 Details of foam filled extrusion S-T4-5-1.7-2-1

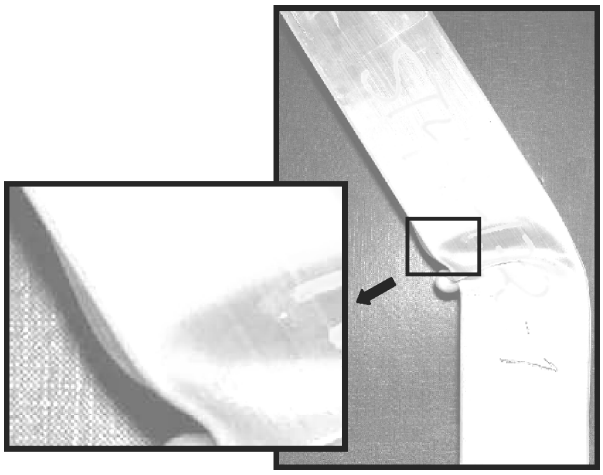

As given in Figure 18 for non-filled extrusions, the force-deformation curve rapidly drops compared to pure axial crushing. This was also observed for foam filling. Figure 21 shows how the mean crushing force drops as a function of loading angle ($\theta = 0°$ refers to pure axial crushing) for tempers T4 and T6.

Figure 21 Mean load at $d = 50$ mm vs. load angle. The calculated mean crushing force for an axially loaded column is also included

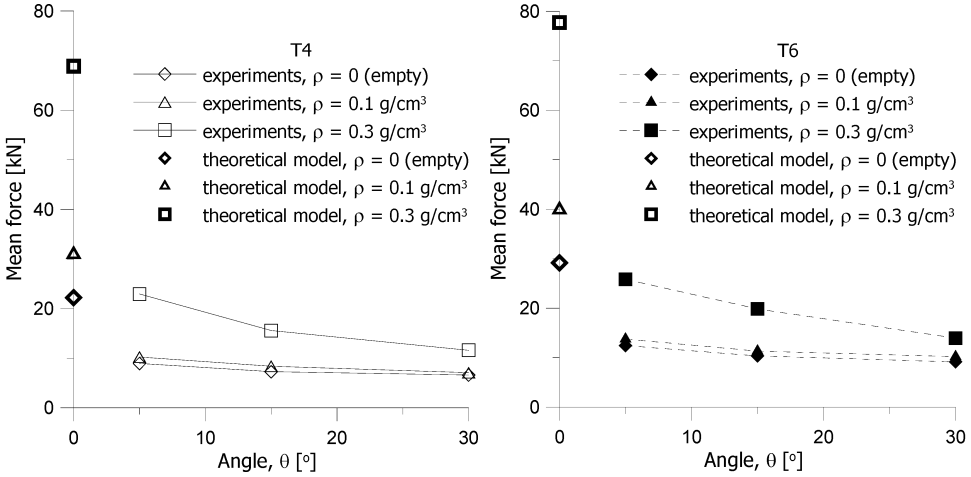

The plastic hinge over the cross section of obliquely loaded members will be subjected to both axial force N and bending moment M. Reyes et al. (2004a) plotted the axial force and bending moment occurring in the plastic hinge for the same rotation and obtained interaction curves, see Figure 22 for foam filled T4 and T6 extrusions. Note how the interaction envelopes shrink as the deformation proceeds, reflecting the softening behaviour of the obliquely loading member as given in Figure 18.

Figure 22 Interaction plots for obliquely loaded foam-filled extrusions

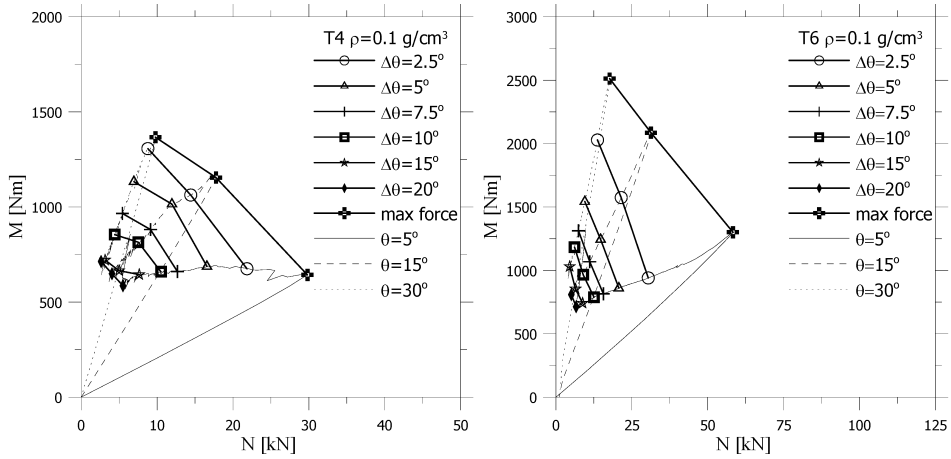

3.3 Three-point bending

Hanssen et al. (2000b) did three-point-bending tests on three different aluminium extrusions with foam filler. The extrusions were square-hollow sections of alloy AA6060. Figure 23 shows what happens to an AA6060 temper T6 beam when increasing the foam filler density. The graphs show the moment vs. rotation M-φ plots corresponding with the photos. Two parallels were carried out (test a and b). The top test B10 refers to the non-filled extrusion. Foam filler density increases downwards in the figure.

Introducing the lightest foam filler to the beam significantly altered the deformation behaviour, as shown by the photographs in Figure 23. First of all, the plastic hinge in the middle of the beams has become less influenced by the geometry of the indenter. For comparison, the deformation pattern of the non-filled beams was clearly determined by the rather large, inward bulge generated by the blunt nose of the testing machine. Another observation is that the plastic hinge is very concentrated when applying the low density foam filler ρ_1.

The foam filler also had a pronounced effect on the initial peak moment M_s of the beams, resulting in increased capacity, see Figure 23. The explanation to this observation is twofold. First, the foam filler itself has a structural capacity that increases nonlinearly with the density of the foam, see Figure 2. Secondly, the foam filler acts as a support for the sidewalls of the extrusions, significantly increasing the local buckling load. This was also observed in Section 3.1 for the axial crushing of foam filled columns. Comparing the photographs of the beams with the highest densities (B12 and B13) with the low-density filler beams (B11) shows that the sidewall lobe size is reduced by increasing the foam filler density. This is a direct result of the initial buckling taking place on a semi-elastic foundation, leading to reduced buckling lengths as the stiffness of the foundation is increased.

The initial drop in capacity appears to increase as the foam filler density increases. The reason is that the initial peak load now is determined by the failure strain in tension of the foam filler. When this failure strain is reached, the fracture propagates and divides the entire cross section of the foam filler. Hence, the drop in capacity should more or less equal the load bearing capacity of the foam filler.

Figure 23 Test results, beam B1 (Temper T6, h = 1.76 mm)

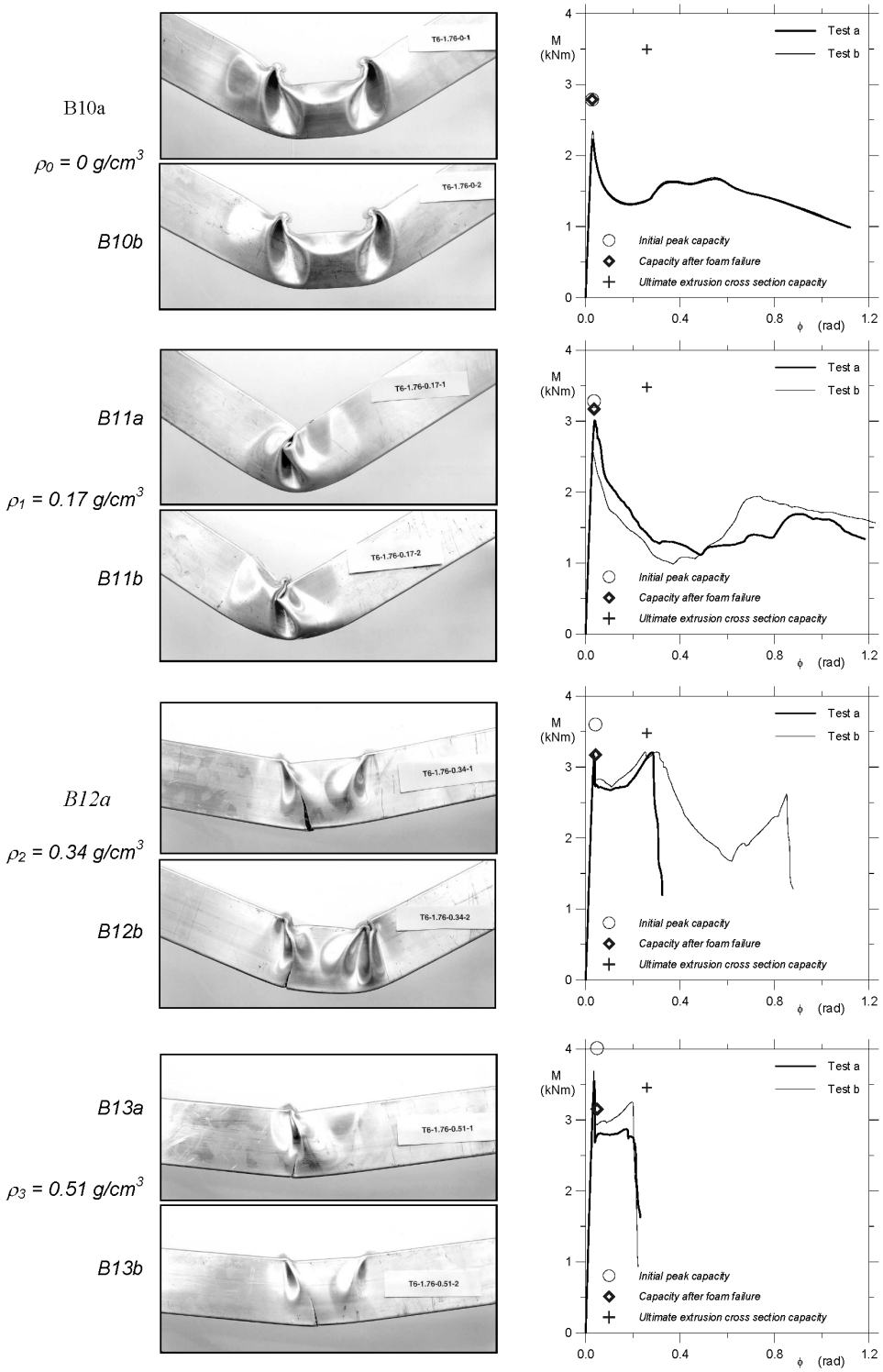

As seen from the photographs in Figure 23, the medium and high-density foam beams (ρ_2 and ρ_3) eventually failed due to ductile failure in the tensile flange of the extrusions. When pure bending occurs, as for the specimens tested herein, the compressive flange has to balance the stresses in the tensile flange, otherwise axial forces would be present. For the non-filled and low density filled beams ρ_1, rather mature lobes are generated in the compressive zone as a result of the initial local buckling. The compressive force required to develop these lobes are so low that the balancing stresses in the tensile zone of the extrusion do not exceed the stress corresponding to the failure strain. As explained above, the local buckling forces increase as the buckling length gets smaller, as is the case for the high-density foam fillers. This again requires higher stresses in the balancing tensile flange, which eventually may lead to ductile failure.

All in all, the foam filler helps the extruded beams to retain their initial cross sectional shape before and after local buckling has occurred. In addition, the bending resistance of the foam core itself contributes significantly to the initial, elastic capacity of the beams. In the following, simple models predicting the load bearing capacity of the beams will be developed and correlated with the experimental data. Three different stages in the loading path will be considered:

- initial peak load
- load bearing capacity after tensile failure in foam
- ultimate cross section capacity of the extrusion.

The following strategy is applied in order to develop a simple design formula valid for the initial peak load of foam-filled beams. Assume that the foam core helps the cross section to retain its shape during the initial stages of bending, that is: initial buckling is prevented. Hence, for the present case of foam filling, we may assume that buckling only takes place after the foam core fails in tension, a failure that most likely propagates through the whole cross section. Hence, if the failure strain of the foam is known, the corresponding strains in the extrusion can easily be determined and applied for the determination of the moment resistance of the extrusion (based on initial cross section geometry). When added to the moment resistance of the foam core immediately before failure, the total initial peak load may be determined.

Following classical beam theory, the cross section moment M is found by integrating moment contributions from a given stress distribution $\sigma(z)$ over initial cross section geometry

$$M = \int_{A_e} \sigma z dA_e + \int_{A_f} \sigma z dA_f . \tag{22}$$

The stress distribution is determined from the corresponding strain distribution. Equation (22) has been divided into two parts, being integration over the extrusion area A_e as well as integration over the foam core area A_f. Following the same approach as in Section 2.3 and using identical notation (substituting the thickness of the surface skin with the thickness of the extrusion here), this leads to the following design formula for the total bending moment capacity M of the foam filled beams as function of curvature: $M = M_e + M_f$ (M_e is moment contribution from extrusion, M_f is contribution from foam core)

$$\begin{aligned} \frac{M}{M_{02}} &= f\left(1-\frac{E_t}{E}\right)+\frac{E_t}{E}\frac{\kappa}{\kappa_{02}}+\frac{M_{sf}}{M_{02}}\frac{\kappa}{\kappa_s} \quad && M_e > fM_{02} \\ \frac{M}{M_{02}} &= \frac{\kappa}{\kappa_{02}}+\frac{M_{sf}}{M_{02}}\frac{\kappa}{\kappa_s} && M_e \le fM_{02}. \end{aligned} \tag{23}$$

Assuming that the maximum initial capacity of the cross section is obtained at foam failure, the maximum bending moment is found from equation (23) when $\kappa = \kappa_s$. For non-filled beams, the elastic capacity is defined herein by inserting $\kappa = \kappa_{02}$ and $M_{sf} = 0$ in equation (23). Just after the foam core has failed, the moment capacity can be found from equation (23) by inserting $M_{sf} = 0$.

The results by using this formula before ('initial peak capacity') and after foam failure ('capacity after foam failure') are shown in Figure 23. The predicted capacities are plotted for beam rotations determined by additional formulas given in Hanssen et al. (2000b).

Even after foam failure, the cross section may build up a new maximum moment capacity, generating large plastic strains in the extrusion walls. Assume that such a strain distribution can be represented by a stress-strain curve on the form $\sigma = \sigma_u(\varepsilon/\varepsilon_u)^n$. Hanssen et al. (2000b) wrote the ultimate bending moment capacity M_u for a square foam filled extrusion on the form

$$M_u = \frac{1}{(n+2)2^{n+1}}\frac{\sigma_u}{\varepsilon_u}(b^{n+3}-(b-2t)^{n+3})\kappa_u^n, \quad \kappa_u = 2\frac{\varepsilon_u}{b}. \tag{24}$$

As seen in Figure 23 ('ultimate extrusion cross section capacity') this formula works well for high foam densities when the foam filler enables the cross section to retain its shape for large rotations.

4 Finite-element modelling

Finite element modelling of foam-based components requires robust constitutive models. Several material models exist that can be applied for foam. Section 4.1 focuses on one model only, but several others are fully applicable; see Hanssen et al. (2002). One of the most important requirements to a material model for aluminium foam is the model's ability to predict material failure. For many applications, such as crash, failure of foam in tension will lead to rearrangement of the structural forces, which again may lead to failure elsewhere. Section 4.2 will use the model described in Section 4.1 to simulate the three-point-bending tests and failure of the pure foam beams described in Section 2.3. The surface skin (and its failure) is also included in the model. Section 4.3 shows simulations of the obliquely loaded foam-filled extrusions described in Section 3.2. Section 4.4 gives results when using the foam model for representing the three-point bending tests described in Section 3.3. The material model for the hollow extrusion was also able to take into account failure. This foam-filled beam is an interesting example, as it shows the interaction between the failure in the foam core and the failure in the tensile flange of the extrusion.

4.1 The Deshpande-Fleck model

The foam model of Dehspande and Fleck (2000b) has been implemented as a user subroutine in LS-DYNA, see details in Reyes et al. (2003), and is also found as material model 154 in LS-DYNA version 970 (2003). The implemented model includes a simple fracture criterion, and reasonable results have been obtained when this model was applied for verification tests on foam alone, Reyes et al. (2003). The anisotropy of the foam is not taken into account in the foam model.

The yield criterion of the material model is given as

$$\Phi = \hat{\sigma} - Y \leq 0 \tag{25}$$

where

$$\hat{\sigma}^2 = \frac{1}{1+(\alpha/3)^2}(\sigma_e^2 + \alpha^2 \sigma_m^2). \tag{26}$$

Here, σ_m is the mean stress and the parameter α defines the shape of the yield surface. α is a function of the plastic coefficient of contraction, ν^p:

$$\alpha^2 = \frac{9}{2}\frac{(1-2\nu^p)}{(1+\nu^p)}. \tag{27}$$

Since ν^p can be assumed to be zero for the aluminium foams considered in the current study, Reyes et al. (2003), α is equal to $\sqrt{9/2} \approx 2.12$.

The material model includes the following isotropic strain-hardening rule:

$$Y = \sigma_p + R(\hat{\varepsilon}) = \sigma_p + \gamma \frac{\hat{\varepsilon}}{\varepsilon_D} + \alpha_2 \ln\left(\frac{1}{1-(\hat{\varepsilon}/\varepsilon_D)^\beta}\right). \tag{28}$$

Here, $\hat{\varepsilon}$ is the equivalent plastic strain, while σ_p, α_2, γ, ε_D, and β are material parameters. If the strain hardening rule is calibrated to a uniaxial compression test, the compaction strain ε_D can be expressed as, Reyes et al. (2003)

$$\varepsilon_D = -\frac{9+\alpha^2}{3\alpha^2}\ln\left(\frac{\rho_f}{\rho_{f0}}\right) \tag{29}$$

where ρ_f is the foam density and ρ_{f0} is the density of the base material, which is 2.7 g/cm^3 for aluminum. The other material properties, σ_p, α_2, γ, and β, can also be expressed as a function of the foam density:

$$\left\{\sigma_p, \alpha_2, \gamma, \frac{1}{\beta}\right\} = C_0 + C_1\left(\frac{\rho_f}{\rho_{f0}}\right)^n \tag{30}$$

where C_0, C_1, and n are constants, Hanssen et al. (2002).

Material tests were used to determine the power-law relationship between foam density, ρ_f, and foam plateau stress, σ_p, which is expressed in equation (30) with $C_0 = 0$. Furthermore, the values of C_0, C_1, and n in equation (30) for the other material parameters, were assumed to be the same as in previous studies, Reyes et al. (2003).

Fracture is modelled by eroding elements when a fracture criterion is satisfied. One strain-based and one stress-based criterion were implemented in the model.

The strain-based criterion is controlled by the volumetric strain, i.e.

$$\varepsilon_m \geq \varepsilon_{cr}. \tag{31}$$

The second criterion is based on erosion of elements when the maximum principal stress reaches a critical value:

$$\sigma_1 \geq \sigma_{cr} \tag{32}$$

where σ_{cr} is the critical stress. However, because of spurious noise produced by contact forces and elastic stress waves initiated when an element is eroded, the stress levels in the elements can at times be higher than the critical stress, although these should not necessarily cause fracture. To avoid erosion of elements due to spurious noise, an energy-based criterion was established from equation (31) motivated by Cockcroft and Latham (1968). An element is eroded when the 'energy' $\int_0^{\hat{\varepsilon}} H(\sigma_1 - \sigma_{cr})\sigma_1 d\hat{\varepsilon}$ is larger than a user-defined critical value C, i.e.

$$\int_0^{\hat{\varepsilon}} H(\sigma_1 - \sigma_{cr})\sigma_1 d\hat{\varepsilon} \geq C. \tag{33}$$

Here, $H(x)$ is defined as $H(x) = \begin{cases} 1 & \text{if } x \geq 0 \\ 0 & \text{if } x < 0 \end{cases}$.

The simulation results on development of failure and subsequent removal of rather large elements should always be checked for mesh sensitivity.

4.2 Modelling failure in foam and surface skin

This section models the three-point-bending tests of IFAM foam beams presented in Section 2.3. Here the foam blocks were modelled by brick elements and the surface skin represented by shell elements with nodes merged to the nodes of the brick elements in the foam core. For this study tensile properties of the foam's surface skin as well as compression curves of foam samples were needed. The tensile stress-strain curve of the foam skin is difficult to achieve. Attempts to separate the foam skin from a foam sample for tensile testing failed due to pores/holes in the prepared foam skin. Thus the mechanical properties have been approximated by the tensile properties of cast AlSi7 from Dørum et al. (2003), Figure 24 (left). Following this work, the foam skin was modelled with von Mises' yield criterion, associated flow rule and non-linear isotropic strain hardening represented by a generalised Voce hardening rule. Model 104 of LS-DYNA (*MAT_DAMAGE_1) was used to represent the skin. The input card was defined so as to give a failure after 6% effective plastic strain, see Figure 24. The thickness of the surface skin was taken to be 0.15 mm as found analytically in Section 2.3. The compression curve of the investigated foam was generated for square cross-section samples (approximately 53×53 mm) with a length of 100 mm without surface skin. The density of the foam (without skin) was approximately 560 kg/m^3. The compression curve was used to identify the hardening model of material model 154 of LS-DYNA as described in Section 4.1. The LS-DYNA version of this work also includes material failure based on an upper limit of the plastic part of the volumetric strain,

equation (31). The fit of the hardening curve to the experimental tests is given in Figure 24 (right).

Figure 24 Identified material models for surface skin (left) and foam (right)

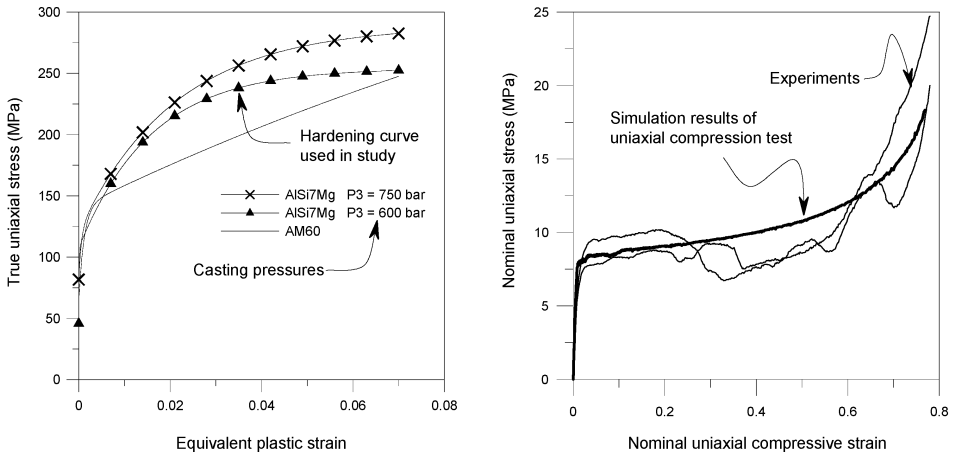

A numerical model of the three-point-bending test set-up was made using the non-linear finite element code LS-DYNA, see Figure 25. The results are given in Figure 26 compared with the experimental curves. A volumetric failure strain of 0.05 was found to comply well with the tests on the pure foam beam (0S), see Section 2.3. Considering the experimental scatter, the CES thickness found by the simple procedure above appears to comply well with the results from simulation of components 3S and 4S.

Figure 25 Finite element model of three-point-bending test set-up

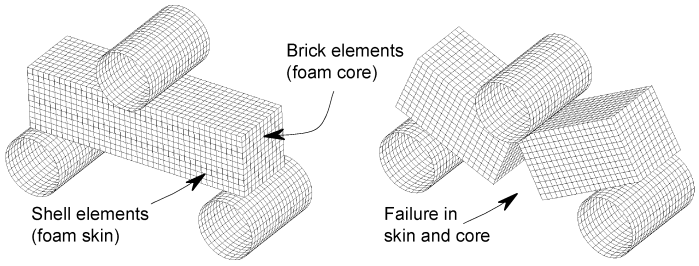

Figure 26 Comparison of num. simulations (LS-DYNA) with exp. results

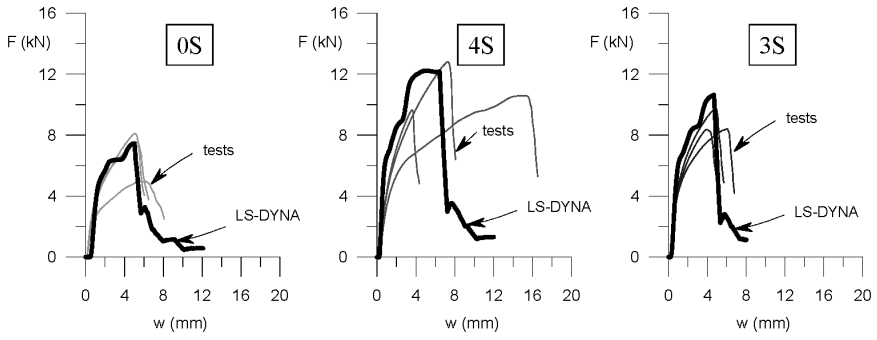

4.3 Simulation of obliquely loaded specimens

Upon simulating the obliquely loaded specimens, all the components collapsed globally, just as in the experiments. In the experiments, quite a number of different deformation modes were seen, but in the analyses mainly two modes occurred, see Figure 27. Deformation mode A** occurred for the columns filled with the high-density foam, while the others experienced mechanism C. Fracture in the foam core occurred for many of the tubes. Figure 27 depicts how the two main deformation modes influence the extrusion and the foam core, and shows how the fracture in the foam is developed close to the clamping. The foam also fractured in the corners where the lobes in the extrusions were created in all analyses, see Figure 28.

Figure 27 Pictures from the analyses: extrusion, foam core and fracture

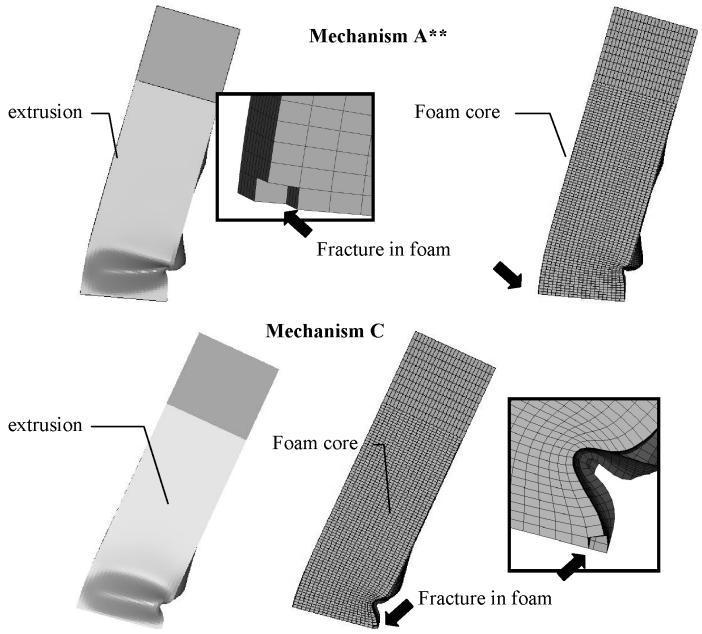

Figure 28 The development of fracture in the foam, in the corner where the lobes in the extrusions were created

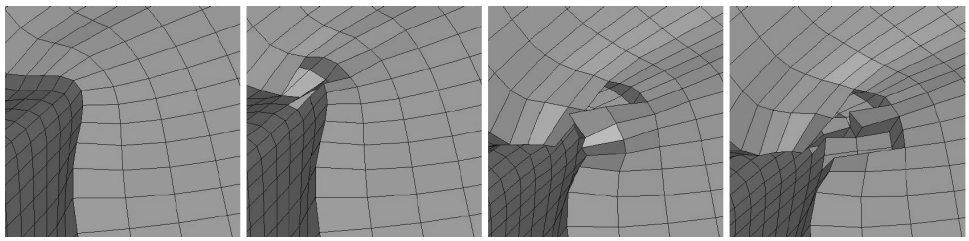

Typical force-deformation curves from the simulations are given in Figure 29 for different foam-filler densities. A correlation plot is also given here, showing that the numerical simulations on overall underpredicted the experiments somewhat.

Figure 29 Numerical force-deformation curves (left) and correlation plot (right)

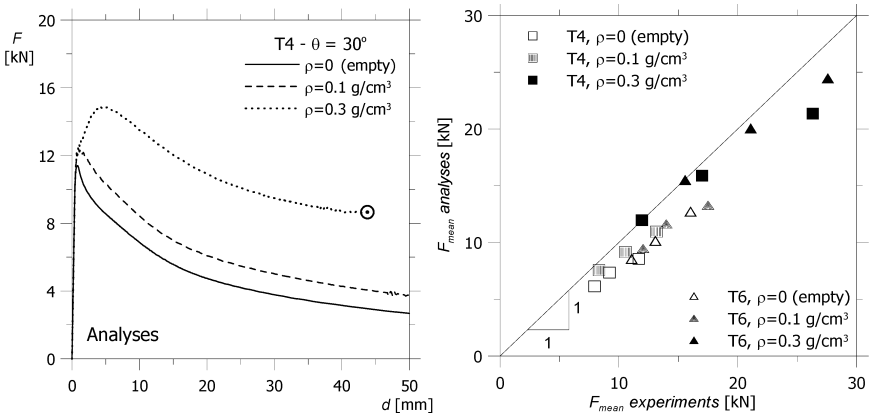

Figure 30 shows that modelling the fracture and statistical variation of foam density had little influence on the results. Initial imperfections in the extrusion walls lowered the peak loads by a small amount only.

Figure 30 Difference between analyses with and without initial imperfections, and the analyses with statistical variation and with or without fracture

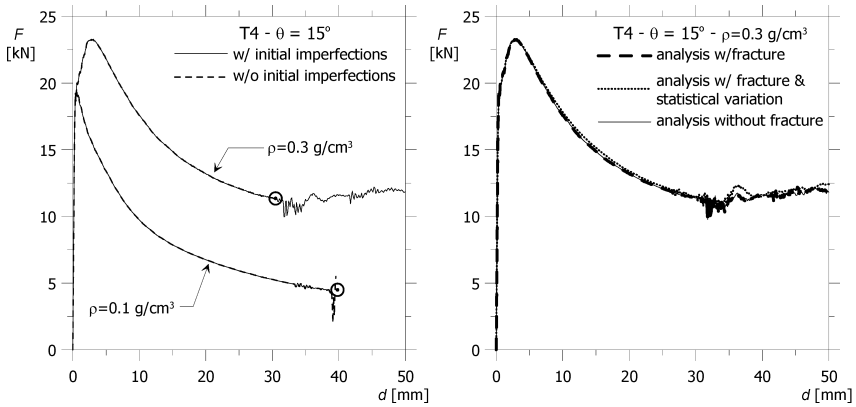

The symbol ⊙ indicates where the analyses were stopped due to numerical problems

4.4 Three-point bending of foam-filled extrusion

The finite element model of the test set-up and section view of the specimens can be seen in Figure 31, based on Reyes et al. (2004b). In the experiments, wooden blocks were placed in the beam ends to prevent the foam filler to move axially when loaded. The wooden inserts were jointed to the beam ends by bolts, but in some tests the joints failed and the inserts were pushed outwards by the foam. In order to take this into account in the analyses, two simulations were always carried out for each beam type. In the first, the foam was completely free to move out of the extrusion ends, in the second the foam's movement was restricted by the introduction of end covers. It was found that when the foam was free to move out of the beam in the model, there was no initiation of fracture in the extrusion material. Furthermore, all the foam-filled beams with covers at

the ends were analysed using two fracture criteria for the extrusion material and two fracture criteria for the foam (equations (31–33)). For the extrusion the fracture criteria used were

- a criterion based on thickness strain, here referred to as CFS* (Reyes et al., 2004b)
- the Cockcroft-Latham criterion abbreviated by CL (Reyes et al., 2004b).

For the foam, the strain- and stress-based criteria are called ‘fr1’ (equation (31)) and ‘fr2’ (equation (33)) respectively.

Figure 31 FE model of the three-point-bending tests. Half of the beam was modeled (top) and symmetry conditions applied. The meshes of the foam (middle) and the extrusion (bottom)

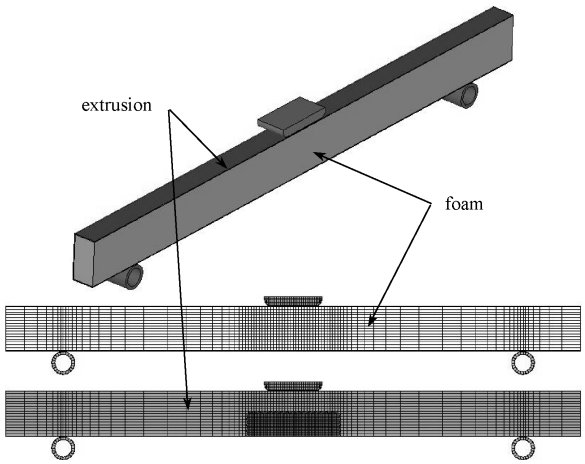

Figures 32 and 33 show force-displacement curves and representative pictures from experiments and analyses of the lowest and highest density foam-filled beams of Figure 23 (Section 3.3). Most of the pictures from the analyses are taken at approximately the time that corresponds to the maximum deformation from the experiments. Sections of the beam from the analyses are also shown so the foam behaviour can be observed. In the pictures, the foam is coloured lightly, while the dark colour represents the extrusion.

Figure 32 FE simulations of three-point bending of AA6060 T6 beam with low-density foam filler

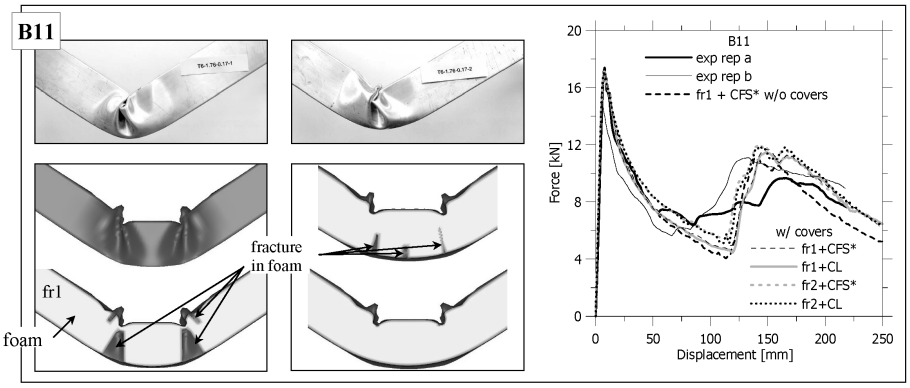

Figure 33 FE simulations of three-point bending of AA6060 T6 beam with high-density foam filler

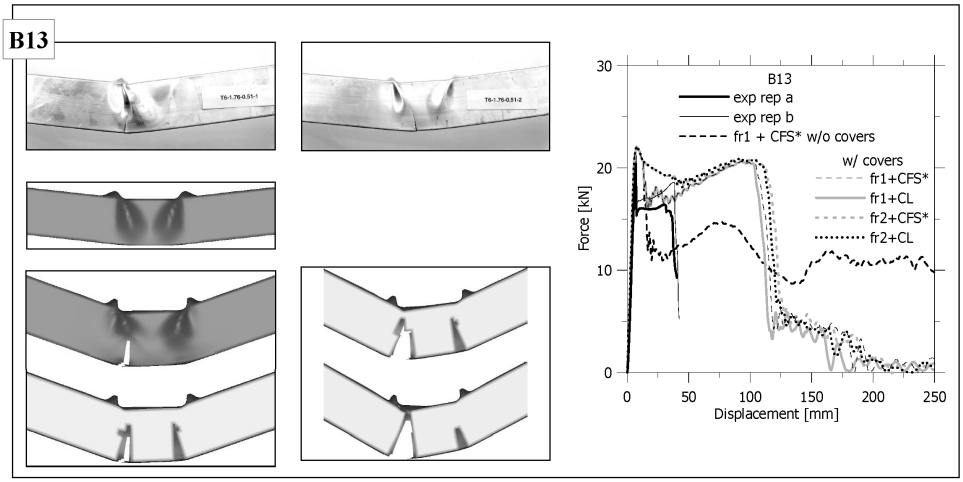

As can be seen from the simulations, the foam fractures for the low-density beams, but fracture does not develop in the extrusion, as observed experimentally. For the high-density beams, fracture occurs in the tensile flange of the extrusion subsequent to the failure of the foam core. This is also in agreement with experimental results. However, as seen from the force-deformation curve of Figure 33, failure of the extrusion material in the high-density foam beams occurs much later than in the experiments. There is also little difference between the various material failure criteria used.

5 Conclusions

A general summary of existing work on generic foam-based components for crashworthiness applications have been given. Where available, design formulas have been added. Several of the experimental results presented have been the basis for comparison with finite element simulations. It appears that foam-filled structures pose a considerable challenge when it comes to finite element modelling as the foam filler will directly influence the behavior of the surrounding material. Here, the paper has demonstrated by several examples that failure of aluminum foam in parts subjected to tensile stresses must be captured in order to predict the overall response of the structure well.

Acknowledgements

This work has been carried out with support from the Norwegian Research Council through the Strategic University Program “Design of Crashworthy Light-Weight Structures” and the research program NorLight on the crashworthiness of light-weight structures.

References

Banhart, J. (2001) 'Manufacture, characterisation and application of cellular metals and metal foams', *Progress in Materials Science*, Vol. 46, pp.559–632.

Cockcroft, M.G. and Latham, D.J. (1968) 'Ductility and the workability of metals', *Journal of the Institute of Metals*, Vol. 96, pp.33–39.

Deshpande, V.S. and Fleck, N.A. (2000a) 'High strain rate compressive behaviour of aluminium alloy foams', *Int. J. Impact Engineering*, Vol. 24, pp.277–298.

Deshpande, V.S. and Fleck, N.A. (2000b) 'Isotropic models for metallic foams', *Journal of the Mechanics a. Physics of Solids*, Vol. 48, pp.1253–1283.

Dørum, C., Hopperstad, O.S., Lademo, O-G. and Langseth, M. (2003) 'Aluminium and magnesium castings – experimental work and numerical analyses', *Int. J. Crashworthiness,* Vol. 8/2, pp.455–470.

Hanssen, A.G., Hopperstad, O.S. and Langseth, M. (2000b) 'Bending of square aluminium extrusions with aluminium foam filler', *Acta Mechanica*, Vol. 142, Nos. 1–4, pp.13–31.

Hanssen, A.G., Hopperstad, O.S., Langseth, M. and Ilstad, H. (2002) 'Validation of constitutive models applicable to aluminium foams', *International Journal of Mechanical Sciences*, Vol. 44, pp.359–406.

Hanssen, A.G., Langseth, M. and Hopperstad, O.S. (2000a) 'Static and dynamic crushing of square aluminium extrusions with aluminium foam filler', *Int. J. Impact Eng.*, Vol. 24, pp.347–383.

Hanssen, A.G., Langseth, M. and Hopperstad, O.S. (2000c) 'Static and dynamic crushing of circular aluminium extrusions with aluminium foam filler', *Int. J. Impact Eng.*, Vol. 24, pp.475–507.

Hanssen, A.G., Langseth, M., Stöbener, K. and Rausch, G. (2003) 'Closed surface skin of IFAM foams in numerical simulation and verification with experimental results', in Banhart, J., Fleck, N.A. and Mortensen, A. (Eds.): 'Cellular metals: manufacure, properties and applications', *Proceedings of the 3rd International Conference on Cellular Metals and Metal Foaming Technology (2003) Berlin (Germany)*, June, pp.23–25, 363–368.

Jones, N. (1989) *Structural Impact*, Cambridge University Press, Cambridge.

Lopatnikov, S.L., Gama, B.A., Haque, M.J., Krauthauser, C., Gillespie, J.W., Guden, M. and Hall, I.W. (2003) 'Dynamics of metal foam deformation during Taylor cylinder-Hopkinson bar impact experiment', *Composite Structures*, Vol. 61, pp.61–71.

LS-DYNA Keyword User's Manual (2003) Livermore Software Technology Corporation, Version 970, February.

Reyes, A., Hopperstad, O.S. and Langseth, M. (2004a) 'Aluminum foam-filled extrusions subjected to oblique loading: experimental and numerical study', *International Journal of Solids and Structures*, Vol. 41, pp.1645–1675.

Reyes, A., Hopperstad, O.S., Berstad, T., Hanssen, A.G. and Langseth, M. (2003) 'Constitutive modeling of aluminum foam including fracture and statistical variation of density', *European Journal of Mechanics A/Solids*, Vol. 22, No. 6, pp.815–835.

Reyes, A., Hopperstad, O.S., Hanssen, A.G. and Langseth, M. (2004b) 'Modeling of material failure in foam-based components', *International Journal of Impact Engineering*, Vol. 30, pp.805–834.

Tan, P.J. and Reid, S.R. (2000) 'Dynamic characterisation of 'hydro' aluminium foams subjected to high strain rate compression', *UMIST Report ME/AM10.00/NTNU2*.